OPEN ACCESS

University of BRISTOL

Hargreaves, J., Moore, S., Yuan, G., Liu, D., Tipping, H., Abbott, R., Tufnail, J., Dawson, H., & Martin, T. L. (2023). Microstructural modelling and characterisation of laser-keyhole welded Eurofer 97. *Materials and Design*, *226*, [111614]. https://doi.org/10.1016/j.matdes.2023.111614

Publisher's PDF, also known as Version of record

License (if available):
CC BY

Link to published version (if available):
10.1016/j.matdes.2023.111614

Link to publication record in Explore Bristol Research
PDF-document

This is the final published version of the article (version of record). It first appeared online via Elsevier at https://doi.org/10.1016/j.matdes.2023.111614 . Please refer to any applicable terms of use of the publisher.

University of Bristol - Explore Bristol Research
General rights

This document is made available in accordance with publisher policies. Please cite only the published version using the reference above. Full terms of use are available:
http://www.bristol.ac.uk/red/research-policy/pure/user-guides/ebr-terms/

Materials & Design 226 (2023) 111614

Contents lists available at ScienceDirect

Materials & Design

journal homepage: www.elsevier.com/locate/matdes

Microstructural modelling and characterisation of laser-keyhole welded Eurofer 97

J. Hargreaves [a,*], S. Moore [a], G. Yuan [a], D. Liu [a], H. Tipping [a], R. Abbott [a], J. Tufnail [a], H. Dawson [b], T.L. Martin [a]

[a] University of Bristol, H.H. Wills Physics Laboratory, Tyndall Avenue, Bristol BS8 1TL, UK
[b] UKAEA, Culham Centre for Fusion Energy, Culham Science Centre, Abingdon, Oxfordshire OX14 3DB, UK

HIGHLIGHTS

- Thermal analysis and precipitate kinetics modelling were used to predict the microstructure of a Eurofer 97 laser-keyhole weld.
- Microstructural models were validated against characterisation of a weld sample via scanning electron and high-speed atomic-force microscopy.
- Large void defects were discovered in the weld zone, likely caused by Cerium-rich oxide inclusions in the parent material.

GRAPHICAL ABSTRACT

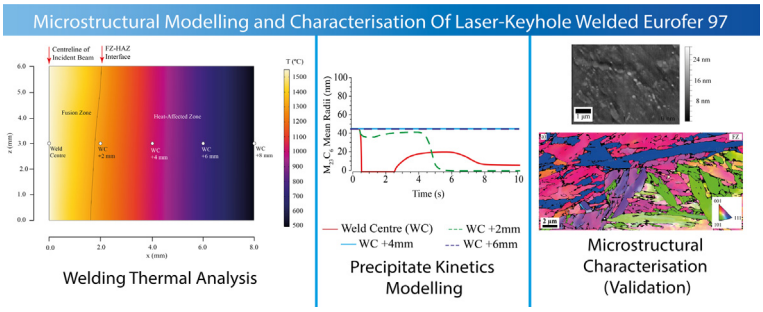

ARTICLE INFO

Article history:
Received 11 November 2022
Revised 20 December 2022
Accepted 9 January 2023
Available online 10 January 2023

Keywords:
Microstructure
Welding
Precipitation kinetics
Analytical electron microscopy
Atomic force microscopy

ABSTRACT

The novel reduced activation ferritic/martensitic steel Eurofer 97 is employed by many concept designs for the plasma-facing first wall of the EU DEMO fusion reactor. These designs feature precision joints between Eurofer 97 coolant piping, for which an advanced laser-keyhole welding technique is proposed. In this work the microstructure of these novel laser-keyhole Eurofer 97 welds is modelled by combining finite element thermal analysis with precipitate kinetics modelling. Microanalysis of a representative specimen via scanning electron and high-speed atomic force microscopy techniques is also conducted, complimented by electron backscatter diffraction, energy-dispersive X-ray spectroscopy, and nanoindentation hardness testing. Models of the weld microstructure agree well with the results of microanalysis although the precipitate diameters predicted are slightly underestimated. Several large void defects were discovered within the weld fusion zone, the cause of which is suspected to arise from the evaporation of cerium-rich oxide inclusions present in the as-cast Eurofer 97 during welding.
© 2023 The Authors. Published by Elsevier Ltd. This is an open access article under the CC BY license (http://creativecommons.org/licenses/by/4.0/).

1. Introduction

Eurofer 97 is a reduced activation ferritic/martensitic (RAFM) modified 9Cr steel developed for structural applications in magnetic confinement fusion reactors. Its reduced activation composition (Table 1) has been developed to alleviate the radioactive waste disposal requirements of reactor decommissioning by substituting elements which may be transmuted into long-lived radionuclides by 14.1 MeV fusion neutrons [1]. While primarily intended for fusion structural applications, Eurofer 97 is also a promising structural material candidate for Gen IV fast fission reactors, fusion-fission hybrid reactors, and spallation neutron sources [2,3].

Eurofer 97 is the reference structural material of the European Union's prototype commercial-scale fusion power station project, the DEMOnstration Fusion Power Station (DEMO) [7]. DEMOs plasma-facing first wall (FW) is likely to be comprised of a modular welded Eurofer 97 structure with plasma-facing surfaces protected

* Corresponding author.
E-mail address: james.hargreaves@bristol.ac.uk (J. Hargreaves).

https://doi.org/10.1016/j.matdes.2023.111614
0264-1275/© 2023 The Authors. Published by Elsevier Ltd.
This is an open access article under the CC BY license (http://creativecommons.org/licenses/by/4.0/).

Table 1
Compositions of Eurofer 97 and the Mod. 9Cr-1Mo steel ASTM P91, a conventional ferritic/martensitic 9Cr steel [5,6]. Minor constituents omitted.

Element	Composition (wt.%)	
	Eurofer 97	ASTM P91
Cr	8.50–9.50	8.50–9.50
C	0.09–0.12	0.08–0.12
Mn	0.20–0.60	0.30–0.60
V	0.15–0.25	0.18–0.25
Ta	0.05–0.15	–
W	1.00–1.20	–
Mo	<0.001	0.85–1.05
Nb	<0.001	0.06–0.10
Ni	<0.030	0.22–0.40

by tungsten armour. Active cooling of the FW via a series of double-wall tubes and embedded channels is envisioned, using either pressurised water or helium. The water-cooled lithium–lead blanket concept (Fig. 1) is one of the leading candidates for DEMO's FW [8].

DEMO's FW must integrate the tokamak's tritium breeding blanket, provide radiological shielding for its magnet systems, and remove useful heat from the fusion plasma for raising steam and generating electricity [11]. Due to the risk of water-lithium interaction, it will be a safety–critical component requiring exacting fabrication [5,12]. Previous research on the fusion welding of RAFM steels using conventional techniques (e.g. gas tungsten inert welding) found that the welds produced exhibit a high degree of hardness, and are susceptible to type IV cracking and reheating cracking [13,14]. This has been attributed to the high matrix carbon content of the welded region caused by carbide dissolution during the period of high temperature [14]. This cracking susceptibility has prompted interest in the use of electron beam welding (EBW) and laser welding techniques for these materials, which produce smaller weld regions that are more readily subjected to post-weld heat treatment (PWHT) [8,15]. Laser keyhole welding (LKW) is presently considered the preferred joining technique for the fabrication of the DEMO WCLL, due to its lower levels of induced deformation, smaller fusion/heat-affected zones, and ability to join thick sections in one pass [16]. This novel welding technique uses high-power millisecond laser pulses to melt a relatively small keyhole region in the weld zone, reducing the overall energy input to the weld material and minimising its residence time at elevated temperature [17].

During service in the DEMO FW, these novel welds may be subjected to high transient thermal loads and intense neutron irradiation fluxes [18]. Joints in water-cooled designs may also suffer from creep, corrosion and irradiation-assisted stress corrosion cracking (IASCC) [8]. While the microstructure and degradation mechanisms of conventional 9Cr steel welds are well understood [6,19], Eurofer 97′s reduced activation composition may give rise to accelerated degradation in the challenging fusion environment. To ensure the integrity of these novel welds during service, there is significant interest in both fully characterising their microstructure, and developing microstructural models that can be used to predict their degradation behaviour [20,21]. To-date, research on LKW Eurofer 97 welds has focused on development of the welding process and the post-weld heat treatment (PWHT) [16,22]. This study combines computational modelling techniques with microstructural analysis of a representative LKW Eurofer 97 specimen to explore the microstructure of these novel Eurofer 97 laser welds in new detail, and predict the evolution of Eurofer 97′s precipitates during welding.

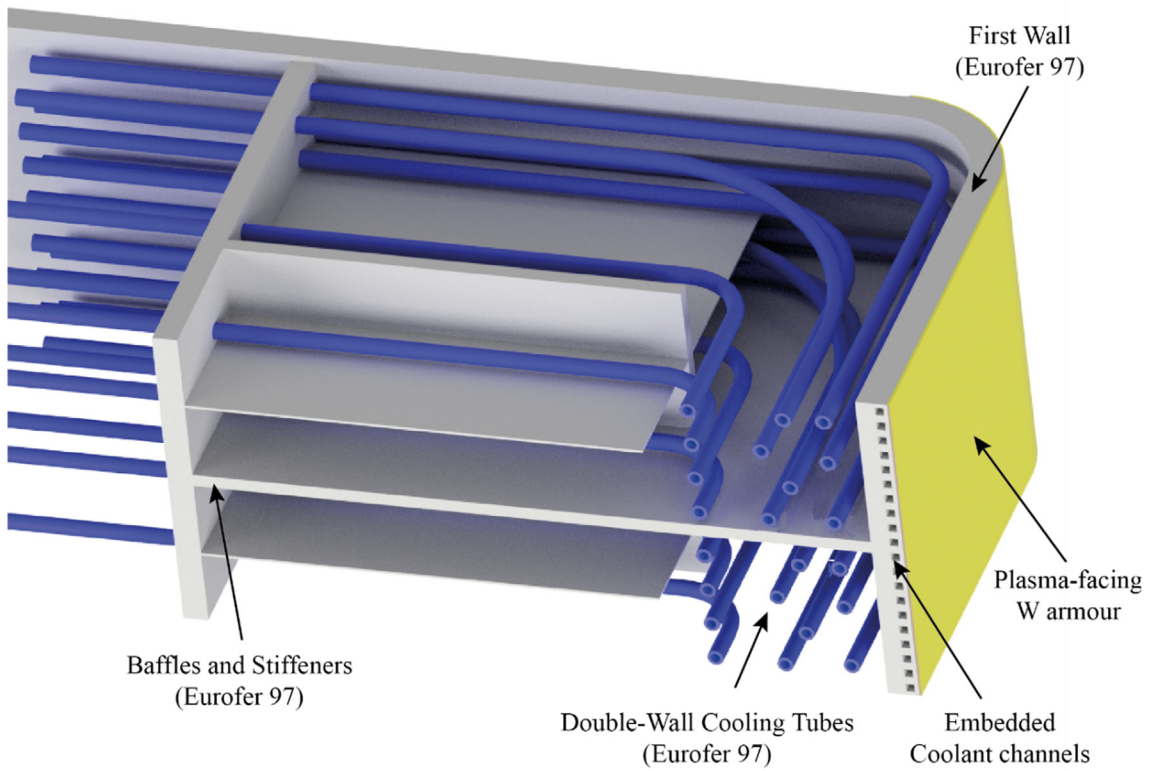

Fig. 1. Annotated 3D model cross-section through the 2019 Single Module Segment (SMS) Water Cooled lithium lead (WCLL) tritium breeding blanket concept design for EU DEMO [9,10].

2. Experimental

2.1. Finite element thermal analysis

Temperatures throughout the welded region during laser-keyhole welding were predicted by time-dependent finite element thermal analysis (FETA) simulations using COMSOL Multiphysics v5.6. A 3D representation of two 6 mm plates was discretised into 1.1×10^5 tetrahedral heat transfer elements by an adaptive meshing algorithm. The keyhole welding laser as described by UKAEA was represented by a single pass of a moving 6 kW gaussian beam [16,22], and thermophysical properties for Eurofer 97 and efficiencies for the laser-material interaction were taken from the literature (Table 2) [4,23]. Properties for ASTM P91 or P92 steel were substituted where values for Eurofer 97 could not be found [24,25]. Radiative and convective cooling in air to an environment at room temperature was assumed.

2.2. Precipitate kinetics modelling

Precipitate phase evolution during welding was modelled using the FETA results and the CALPHAD-based Matcalc computational thermochemistry software (v6.03). To generate initial precipitate populations a microstructural model of Eurofer 97 in its "as-received" condition was generated per its reference thermomechanical treatment (TMT) [26]. As this TMT traverses several matrix phase stability regions martensite and austenite precipitation domains were configured (Table 3). The active domain was selected using phase-transformation temperatures (M_S, Ae_1, and Ae_3) calculated previously [27].

The precipitate phases chosen (Table 4) was based on Eurofer 97′s phase diagram and a literature review. For clarity, MX-type precipitates were subdivided into tantalum-rich carbides (TaC) and vanadium-rich nitrides (VN). Laves and Z-phase nucleation were treated as special cases and restricted to sub-grain boundary edges and existing precipitates respectively. The precipitate diameters predicted by the as-received model were validated against literature values and was found to agree [29].

Six copies of the microstructural model were subjected to short-term heat treatments based on the thermal analysis results (Fig. 4). The resultant evolution in phase fraction and mean precipitate radii evolution is reported for $M_{23}C_6$ and MX-type precipitates (Figs. 5 and 6 respectively).

2.3. Weld specimen characterisation

A representative specimen of LKW Eurofer 97 was fabricated by the United Kingdom Atomic Energy Authority (UKAEA) by butt-welding two 6 mm plates of Eurofer 97 with a single pass of a 6 kW ytterbium fibre laser (λ = 1060 nm). The welding apparatus employed had a 0.6 mm diameter spot size and a focal length of 200 mm at the top of the weld, and the welding speed (W_s) was 0.5 m min^{-1} [16,22]. Several 25 × 6 × 1 mm samples were cut perpendicular to the weld centreline using a water-cooled diamond disc saw at a feed rate of 0.05 mm min^{-1}. These were resin mounted, ground to a 5 μm finish using progressively finer SiC papers, then polished with 3 μm and 0.25 μm diamond paste as per [30]. Samples were vibro-polished with 50 nm colloidal silica. A sample was etched in 2 % nital for 90 s.

Reflected light optical microscopy (LOM) was conducted on the nital-etched sample using a Zeiss Axioscope 7 microscope with image stitching in the Zeiss Core 3 software. A Zeiss SigmaHD Field Emission Gun Scanning Electron Microscope (FEGSEM) with secondary electron (SE) and angle-selective backscattered electron (AsB/BSE) imaging detectors was employed at 10–25 kV for electron microscopy on etched and non-etched samples. An EDAX energy-dispersive X-ray spectroscopy (EDX) detector was used with a 20 kV beam for elemental assay. Electron backscatter diffraction (EBSD) was conducted using an Oxford Instruments Symmetry S3 detector at a specimen tilt of 70°, beam voltages of 25 kV, and probe currents of 700 nA.

High-speed atomic force microscopy (HS-AFM) was employed using a Bristol Nano Dynamics Scanner Mk5N contact mode HS-AFM instrument, operating at 2 frames per second. A Bruker MSNL-10 type C cantilever was used yielding an estimated resolution of 2–3 nm. The AFM tip was scanned across each sample surface in a raster pattern while the vertical displacement of the cantilever was measured by a laser Doppler vibrometer (LDV). Topographical maps were generated using bespoke software (Bristol Nano Dynamics Ltd, UK) and the Gwyddion SPM software. Hardness testing of the welded region of one sample was also conducted using a Hysitron TI Premier nanoindenter equipped with a Berkovich diamond tip. The applied load ranged from 19.0 to 38.3 mN, and a 10 s dwell time was employed with a load/unload time of 5 s. Hardness testing was performed at room temperature.

Table 2
Summary of the laser beam and thermophysical parameters employed.

Parameter	Symbol	Value	Unit
Beam Power	P	6	kW
Gaussian Beam std. dev.	Σ	0.15	mm
Linear weld speed	W_s	0.5	m min^{-1}
Beam absorption efficiency		25	%
Reflectivity		98	%
Surface emissivity	ε	0.39	
Convective heat transfer coeff.		25	W m^{-2} K^{-1}
Thermal conductivity	k	30	W m^{-1} K^{-1}
Specific heat capacity	C_p	See [4]	J kg^{-1} K^{-1}
Dynamic viscosity	μ	0.0065	Pa s
Coeff. Of thermal expansion	α_i	See [4]	K^{-1}

3. Results

3.1. Finite element thermal analysis

An overview of the FETA simulation and its configuration is shown below (Fig. 2).

A mobile phase-change boundary was used to predict the fusion zone (FZ) width, which was predicted to be 4.8 mm and 3.2 mm at the top (beam facing) and bottom of the workpiece respectively (Fig. 3).

To determine temperature profiles throughout the welded region, virtual temperature probes were placed at the weld centre (WC) and at 2 mm intervals on a line perpendicular to the centrelines of the weld and incident beam. The predicted temperatures are shown in Fig. 4.

The temperature profiles obtained were used to model precipitate evolution in the welded region.

3.2. Precipitate kinetics modelling

The model predicts that during welding, all $M_{23}C_6$ carbides in the fusion zone (weld centre) and some smaller carbides in the HAZ (WC + 2 mm) are fully dissolved (Fig. 5a.). $M_{23}C_6$ carbides are predicted to re-nucleate in these regions during cooling and approach their previous pre-weld phase fraction. However, the mean radii of the newly formed $M_{23}C_6$ carbides in the fusion zone are forecast to be 75 % smaller than those found in the parent material (Fig. 5b). In the HAZ, the mean radii of $M_{23}C_6$ carbides is predicted to drop below 10 nm. This is due to the nucleation of many fine $M_{23}C_6$ precipitates that do not sufficient time to grow

Table 3
Parameters of the precipitation domains employed by the as-received simulation [27,28].

Precipitation Domain	Active Temperature Range (°C)	Grain Diameter (m)		Elongation Factor		Matrix Dislocation Density (m^{-2})
		Grains	Sub-Grains	Grains	Sub-Grains	
Austenite	>387	8.5×10^{-6}	N/A	1:1	N/A	1.0×10^{11}
Martensite	<387	8.5×10^{-6}	1.0×10^{-6}	1:1	5	9.0×10^{13}

Table 4
Precipitate phases evaluated by the model and their nucleation settings. α and γ denote the nucleation site is activated in the ferrite and austenite domains respectively.

Precipitate Phase	Nucleation Sites				Elongation Factor
	Dislocations	Grain Boundaries	Sub-Grain Boundaries	Existing Precipitates	
$M_{23}C_6$	–	α	α	–	1:1
TaC	γ, α	γ, α	α	–	1:1
VN	γ, α	γ, α	α	–	1:1
M_7C_3	α	–	–	–	1:3
Cementite	α	α	α	–	1:3
Laves	–	–	α (edges)	–	1:1
Z	–	–	–	α	1:1

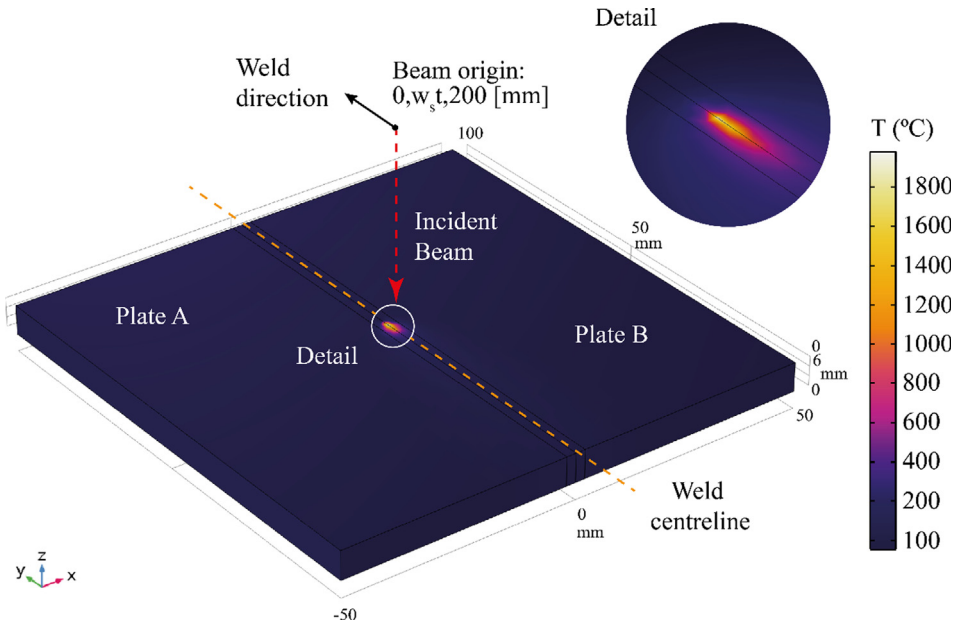

Fig. 2. Finite element thermal analysis (FETA) of the Eurofer 97 laser-keyhole 6 mm plate butt-weld.

appreciably. Beyond WC + 4 mm, all $M_{23}C_6$ carbides were unaffected.

The model predicts that vanadium-rich and tantalum-rich MX-type precipitates (Fig. 6) will exhibit similar trends to the $M_{23}C_6$ phase. Fig. 6a. and 6c. present the predicted phase fractions of TaC and VN precipitates. These show that all TaC and VN precipitates in the fusion zone are predicted to dissolve during welding. Some smaller VN precipitates in the HAZ are also predicted to dissolve, whereas the phase fraction of TaC in the HAZ remains constant. As with $M_{23}C_6$, both types of MX-type precipitates beyond WC + 4 mm were unaffected. The mean radii of the newly formed VN precipitates in the fusion zone is predicted to be 5 nm, approximately half the size of those found in the parent material. The newly formed TaC precipitates in the fusion zone (Fig. 6d) are predicted to have a mean radius of 1–2 nm - considerably smaller than those predicted in the parent material (approx. 16 nm).

3.3. Weld sample characterisation

A stitched optical micrograph of the nital-etched weld region is presented in Fig. 7a. The extents of the FZ and HAZ are delineated clearly. The FZ exhibited an hourglass-like shape with a width (2.7–5.4 mm) slightly smaller than the width predicted by FETA (4.8–6.4 mm). This suggests that temperatures in the welded region may be slightly overestimated by the thermal analysis.

A fully penetrated welded joint is observed with no overlap or excess penetration, however large spheroidal void defects of 0.05–0.25 mm in diameter were discovered in the FZ of several samples. These voids were preferentially located near the weld centreline and at the top of the weld, where the temperature of the weld metal is predicted by FETA to reach a maximum. In some cases, these voids were observed to overlap and join, forming large millimetre-scale cavities (Fig. 7a).

Backscattered electron (BSE) imaging of several voids highlighted spatter-like deposits on their interior surface (Fig. 7b). These deposits were revealed by EDX analysis to be enriched in

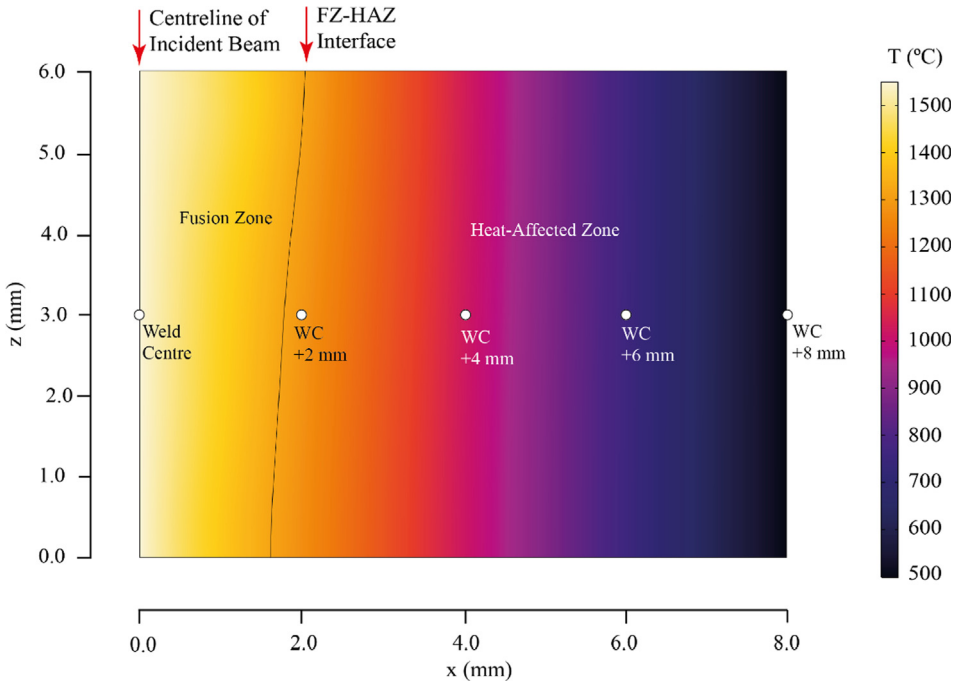

Fig. 3. Cross-section through the centre of the plate (y = 50 mm) at peak temperature, showing FZ-HAZ interface and locations of selected virtual temperature probes (WC + 10 mm omitted for clarity).

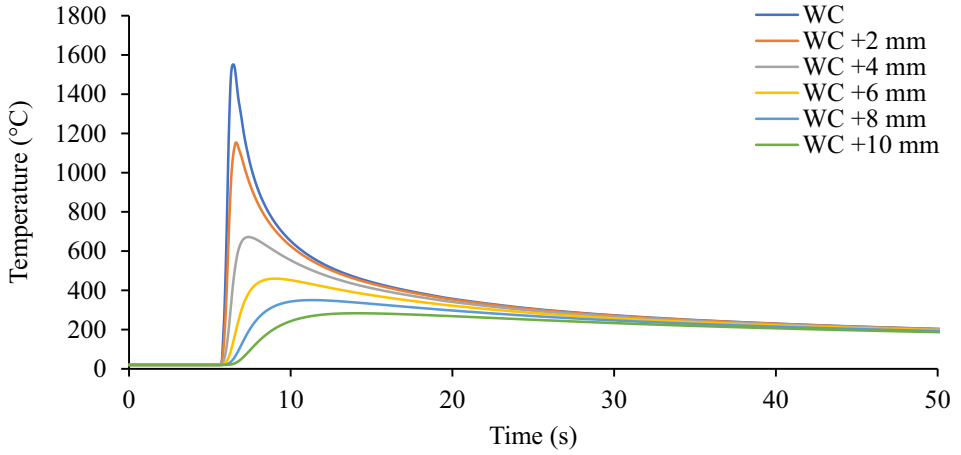

Fig. 4. Predicted temperature profiles during welding at 2 mm intervals from the weld centre (WC).

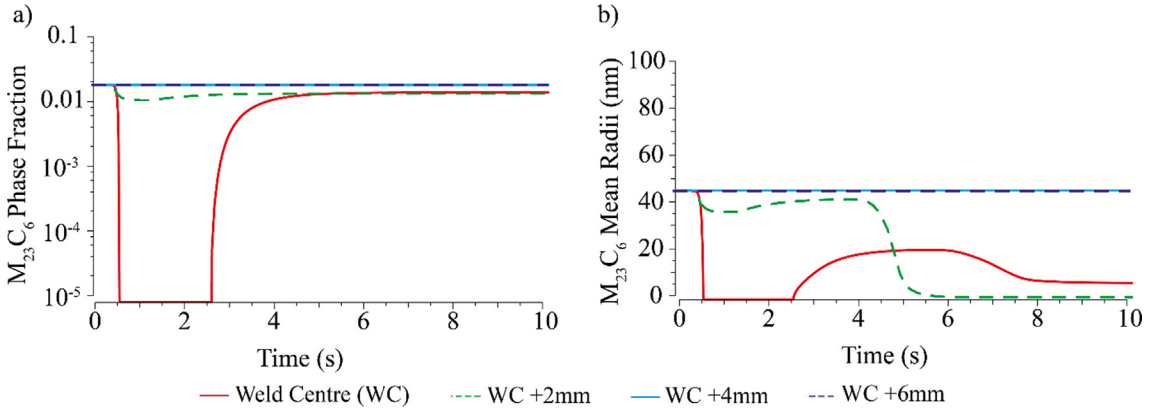

Fig. 5. The predicted evolution of $M_{23}C_6$ carbides in the weld zone during LKW.

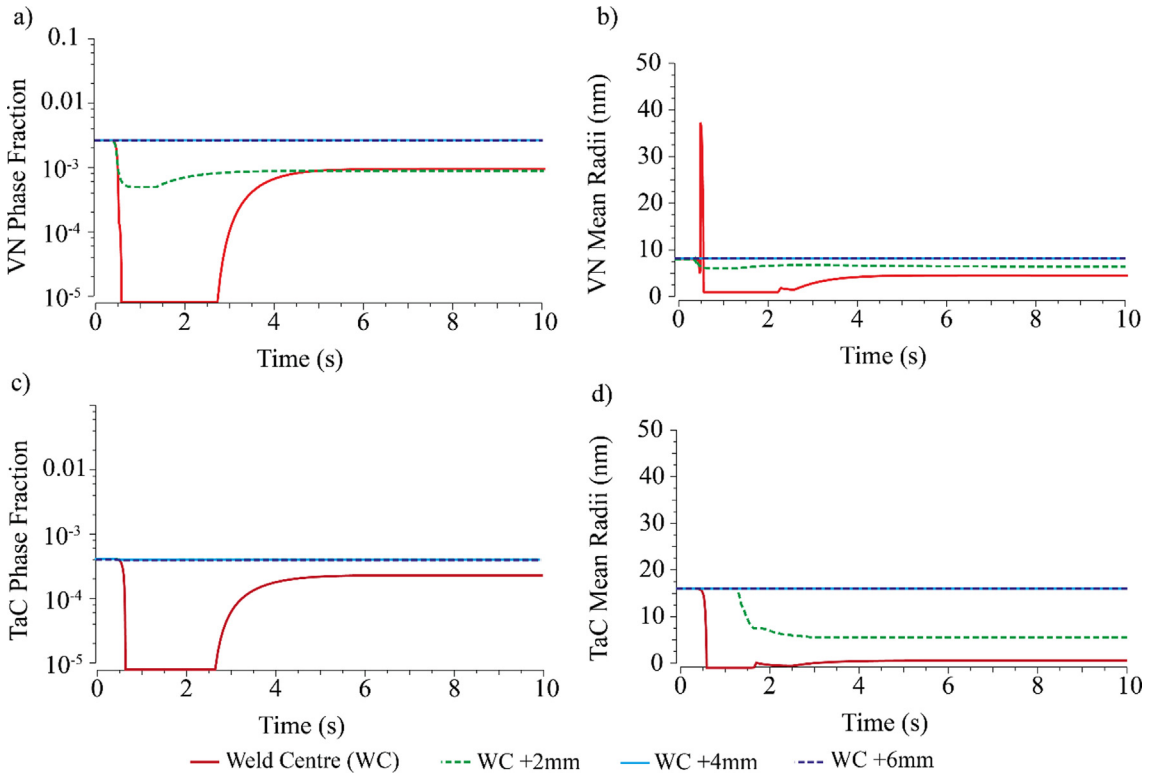

Fig. 6. The predicted evolution of MX-type precipitates in the weld zone during LKW.

both cerium and oxygen. The theorised link between the presence of these Ce-rich oxide deposits and the genesis of the observed voids is elaborated on in the discussion.

Nanoindentation hardness testing was performed on a polished sample free of large voids. The results of the hardness testing are presented in Fig. 7c. The region under test comprised a 5 × 10 mm rectangle about the weld centreline and the centre of the plate. Local hardness was measured at 43 locations spaced 2 mm apart in the parent material, and 1 mm apart in the FZ and HAZ. At each test location a 2 × 3 grid of nanoindentations was made and the average hardness value recorded. A polynomial surface fit to the measured average hardness values is shown.

A typical post-weld hardness profile is observed across the FZ and HAZ, with material in the FZ exhibiting hardness values approximately 2.4 times greater than the parent material. The hardness data obtained corroborates the widths of the FZ and HAZ observed by LOM and predicted by the previously discussed FETA simulation.

SEM and EBSD was employed to study the grain morphology of the welded region. Inverse pole figure (IPF) and kernel average misorientation (KAM) maps collected from the FZ of one weld sample are presented in Fig. 8a, and b, with backscatter electron (BSE) images of lath boundaries (Fig. 8c).

The FZ exhibits a martensitic microstructure comprised of packets and blocks of fine anisotropic laths 6–30 μm in length, nestled within columnar prior austenite grains (PAG) of approximately 40–80 μm diameter. Laths are highly elongated, with aspect ratios ranging from 1:4 to 1:10. Coarse PAG in the fusion zone are epitaxial, and their direction of growth loosely appears to have been away from the weld centre radially along the direction of heat flow. No retained austenite or pearlitic microphases were observed in any region of the FZ. The KAM map of the FZ (Fig. 8b) shows concentrated 'hot spots' of crystalline misorientation located within grains, and at lath boundaries. Some lath boundaries appear to be decorated with fine, highly-elongated precipitates (Fig. 8 c & d). These may be the cause of the crystalline misorientation and the unindexed regions at lath boundaries on Fig. 8a and b.

The HAZ (Fig. 9a,b) was found to consist of a finer heterogenous ferritic/martensitic duplex microstructure. Ferritic grains of up to 4 μm diameter are surrounded by similarly sized packets of lath martensite. The degree of lath elongation in the HAZ is lessened compared with the FZ, with HAZ grain aspect ratios ranging from 1:2 to 1:4. The grain boundaries of the HAZ are decorated by many precipitates, which appear on the EBSD map (Fig. 9a) as unindexed black spots. Precipitate kinetics modelling results (Figs. 5 & 6) suggest that these grain boundary precipitates are likely to be chromium-rich $M_{23}C_6$ type carbides.

The parent material (PAR, Fig. 9c,d) exhibits a normalised and tempered ferritic/martensitic microstructure characteristic of as-received Eurofer 97. Ferritic grains of 4–6 μm diameter are surrounded by coarsened martensitic laths of similar length, with aspect ratios between 1:2 and 1:4. The KAM map shows a lesser degree of crystallographic misorientation in the parent material relative to the HAZ and FZ.

The welded region and parent material were also imaged using high-speed atomic force microscopy (HS-AFM). Selected HS-AFM maps from the FZ and HAZ are shown in Fig. 10.

These images reveal that the fusion zone has a complex martensitic microstructure. Large micron-scale laths are surrounded by packets of very fine nano-scale laths and what appear to be highly elongated precipitates. These precipitates, most likely Cr-rich $M_{23}C_6$, are approximately 20–50 nm wide and are typically orientated parallel to sub-grain (lath) boundaries (SGB). Precipitates in the HAZ are much less elongated and exhibit larger diameters (50–200 nm). These precipitates are generally localised to grain and sub-grain boundaries.

HS-AFM maps of the parent material (Fig. 11) confirm the grain sizes and aspect ratio reported by EBSD and reveal that grain

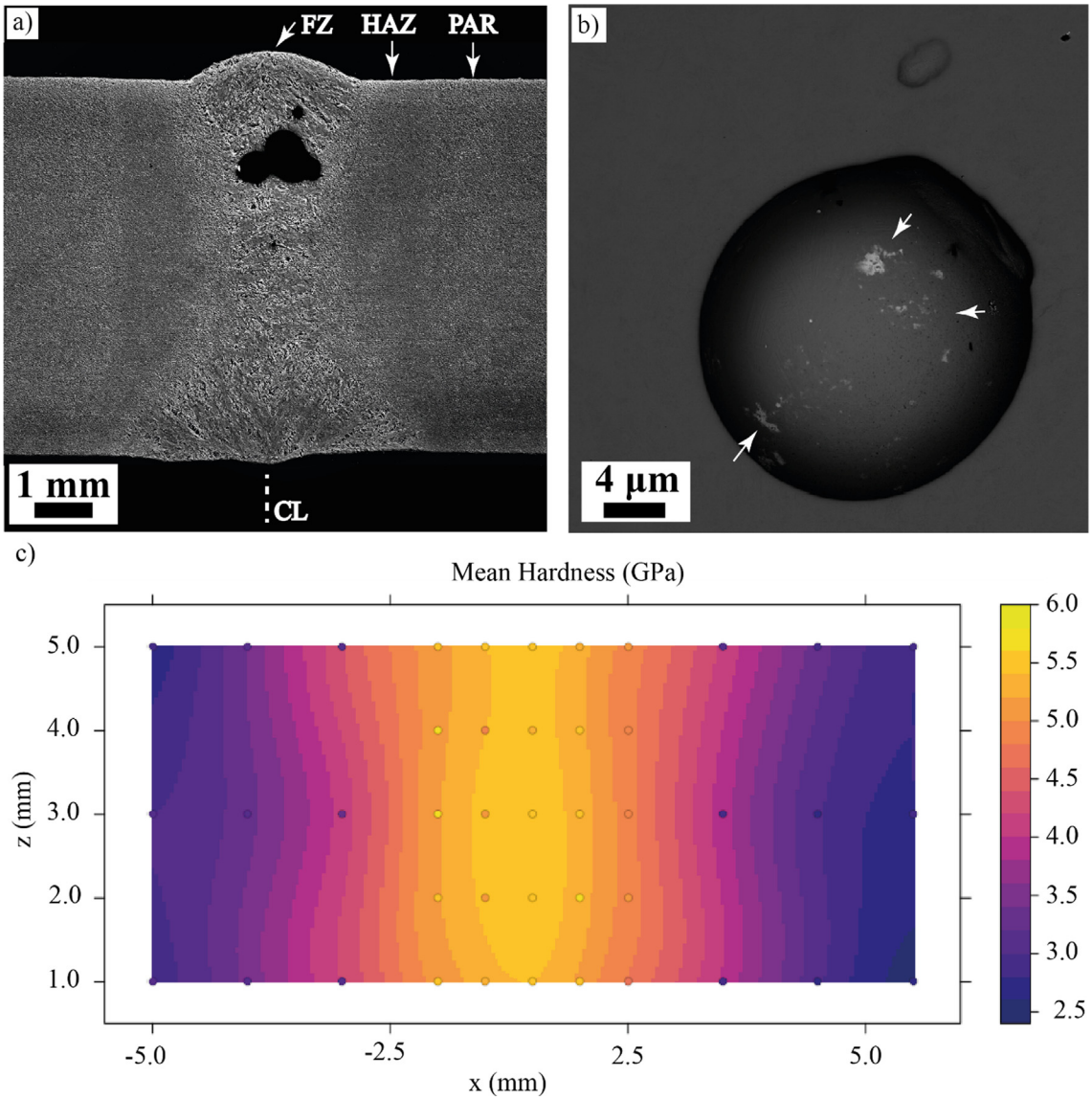

Fig. 7. LOM and AsB micrographs and a hardness map of a cross-section through a LKW Eurofer 97 sample perpendicular to the weld direction a) composite LOM micrograph of the nital-etched sample, b) BSE micrograph of a single large void in the FZ, with arrows pointing to deposits on the void interior, c) nanoindentation hardness map of the welded region.

boundaries are decorated with precipitates approximately 80 nm in diameter. Some matrix precipitates are also observed.

Spheroidal inclusions 1–5 µm in diameter were found to be distributed throughout the parent material and HAZ (Fig. 12a). These exhibited a granular structure and were present in greater number on one side of the weld centreline than the other. Examination of several other non-welded samples likely from the same heat of Eurofer 97 revealed the presence of similar inclusions (Fig. 12b).

EDX analysis of these inclusions (Fig. 13) revealed them to be cerium-rich and co-located with oxygen (O) and vanadium (V) (not shown) suggesting that they are cerium-rich oxides. Inclusions were found to be depleted in both iron (not shown) and chromium (Fig. 13c), suggesting that they have remained in solid form during manufacturing, thermomechanical processing, and welding of the steel. As such, these may be fragments of a crucible or ceramic vessel employed during the steelmaking process.

4. Discussion

The microstructure of a novel laser-keyhole Eurofer 97 butt-weld has been studied using a variety of complementary techniques. FETA was used to estimate thermal fluxes within the welded region during welding and predict the extents of the fusion and heat affected zones (FZ & HAZ). FETA results were employed with phase equilibria and diffusion data to model the evolution of Eurofer 97′s major precipitate phases during the laser-keyhole welding process. To validate the results of modelling, a representative Eurofer 97 laser keyhole weld specimen was characterised via optical, scanning electron, and high-speed atomic force microscopy.

The width of the keyhole weld FZ predicted by FETA was 3.2–4.8 mm, which agrees well with the 2.7–5.4 mm width experimentally observed via LOM (Fig. 7a.). These results corroborate well with the literature on LKW Eurofer 97, which report similar values [22]. The observed FZ is ~60 % smaller than can be achieved by conventional welding techniques such as tungsten inert gas (TIG)

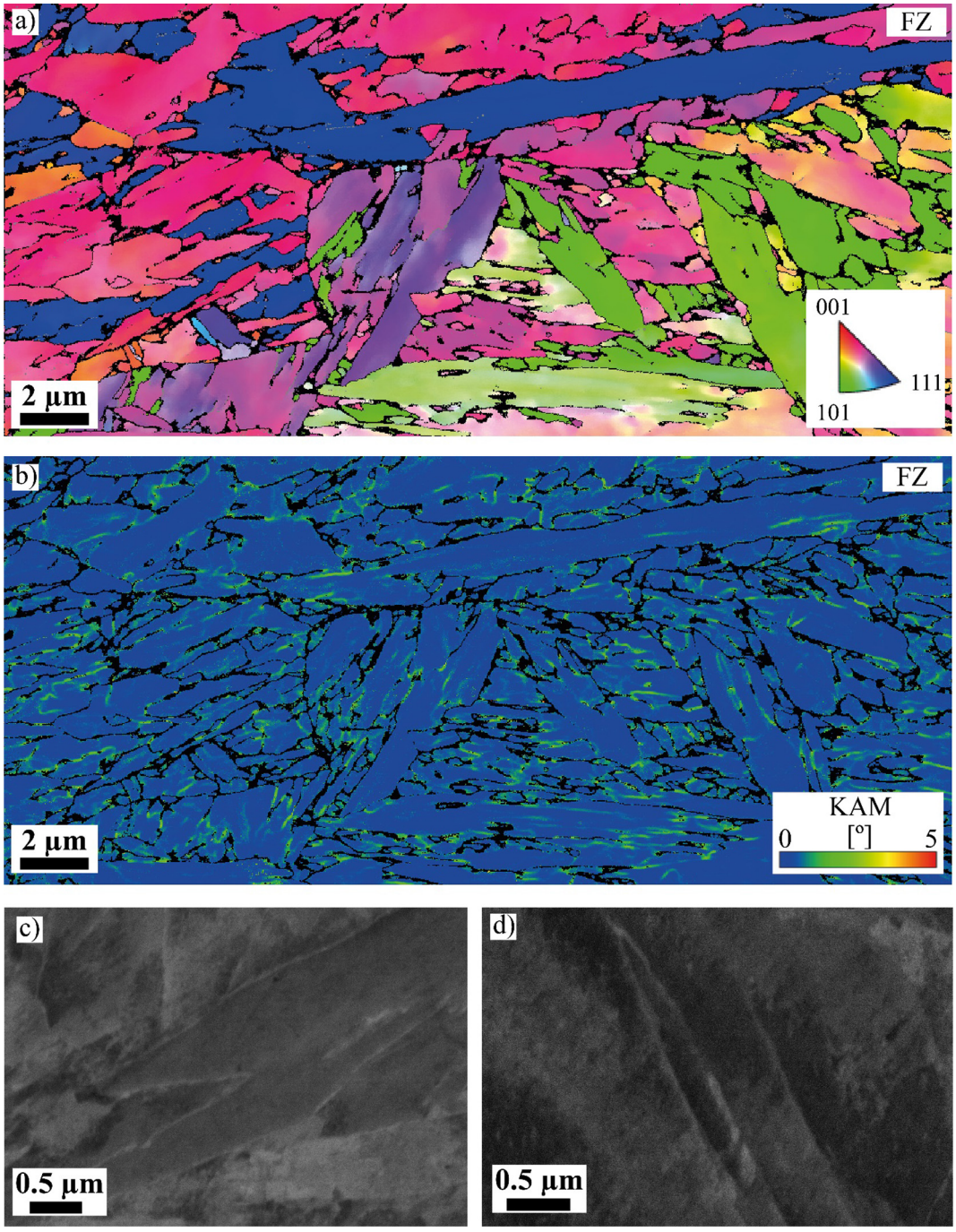

Fig. 8. EBSD maps and AsB images of the fusion zone a) IPF map, b) KAM map, c, d) BSE images of sub-grain (lath) boundaries.

welding [31]. Consequently, the FZ cools very rapidly. FETA predicts the welded region cools at a rate of 5.9 K s^{-1} between Eurofer 97's martensite start (M_s) and end (M_E) temperatures of 370 °C and 210 °C respectively [16]. This is sufficiently fast for the shear-led martensitic transformation to fully complete, which is corroborated by the absence of retained austenite in EBSD maps of the FZ (Fig. 8). The slight discrepancy in the FZ widths estimated by FETA suggests that predicted temperatures in the weld region (Fig. 4) may be slightly overestimated by the simulation. This may be because of conductive thermal losses to a backing plate, which was not considered by the simulation. The accuracy of the thermal analysis results could be improved by including for this and repeating the simulation after measuring the beam-material interaction parameters of the laser welding apparatus. Additionally, data on Eurofer 97's thermophysical properties in the liquid state could be generated and used.

EBSD maps (Fig. 8) show a post-weld microstructure comprised of packets and blocks of lath martensite in the FZ, and a heterogenous HAZ comprised of packets of fine martensitic laths surrounded by larger ferritic grains. Several unindexed regions are evident at grain boundaries. This is either due to the presence of highly-elongated Cr-rich $M_{23}C_6$ precipitates (Fig. 8c and 8d), or grain-boundary dense packets of very fine martensite laths (Fig. 10a). Small grain boundary precipitates in the FZ of LKW Eurofer 97 have been tentatively reported by other authors [22]. The presence of these unindexed areas likely increases the error in

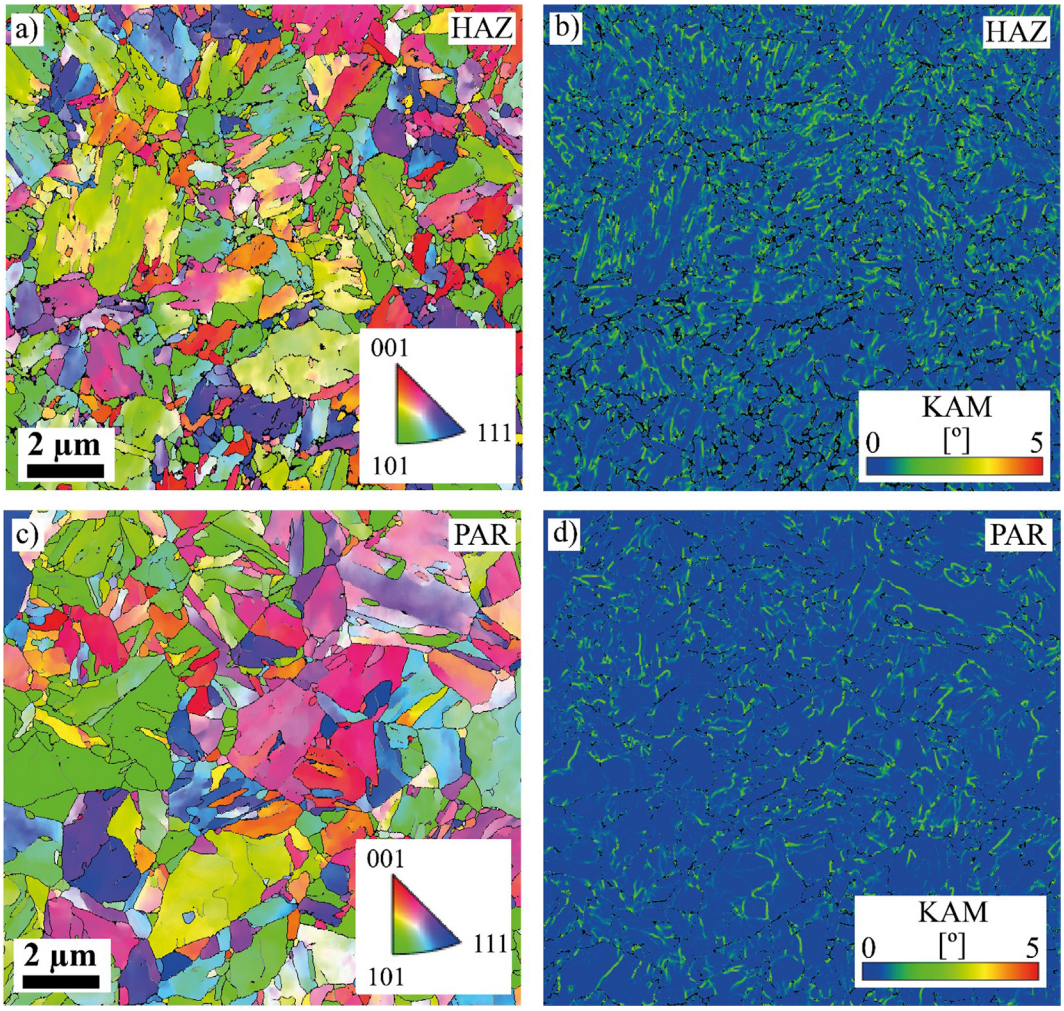

Fig. 9. EBSD inverse pole figure and kernel average misorientation maps of the HAZ (a,b) and parent material (c, d).

grain size measurements. The inter-granular clusters of crystalline misorientation observed on the kernel average misorientation map of the FZ (Fig. 8b) are likely dislocation networks induced during the martensitic transformation, arising from the interstitial trapping of carbon in the super-saturated body-centred cubic (BCC) ferrite matrix. Lath-localised clusters may be the result of residual stresses induced by the shear-led martensitic transformation. The reduced grain boundary density of the HAZ relative to the FZ will result in less dislocation pinning (and thus less Hall-Petch strengthening) which is corroborated by the results of nanoindentation hardness testing (Fig. 10). Hardness testing found that hardness values in the fusion zone are approximately 2.4 times those of the parent material, which agrees with previously published hardness testing data on LKW Eurofer 97 [22].

Precipitate kinetics modelling predicts chromium-rich $M_{23}C_6$ carbide precipitates formed during solidification of the FZ to be 75 % smaller than those found in the parent material (~80 nm mean diameter) while the average radius of $M_{23}C_6$ carbides in the HAZ is predicted to drop below 10 nm. This decrease in the mean radius in the HAZ is not due to precipitates shrinking but was caused by the predicted nucleation of very many small 1–4 nm radius precipitates. These do not have sufficient time at high temperature to ripen appreciably. The existing $M_{23}C_6$ precipitates in the HAZ are predicted to be slightly ripened by welding heat to become 10 % larger.

General trends predicted by precipitate modelling were corroborated by the HS-AFM imaging, which found highly elongated precipitates 20–50 nm wide in the FZ, and larger 50–200 nm dia. precipitates in the HAZ. However, the predicted presence of small sub-10 nm precipitates in the HAZ could not be confirmed. These are either not present, or were too close to the spatial resolution of the HS-AFM instrument to be imaged. The mean precipitate diameters that could be observed by HS-AFM in the HAZ are considerably larger than those estimated by precipitate kinetics modelling. This was likely due to the fixed grain and sub-grain sizes employed for the martensite domain by the model, which poorly represents the complex martensitic microstructure revealed by HS-AFM (Fig. 10a). Future work on precipitate kinetics modelling in martensitic steels should seek to address this by including appropriate models of martensitic grain growth.

The 0.05–0.25 mm diameter voids observed in the FZ constitute a major weld defect as they are likely to act as crack initiation sites during service, and they may coalesce to form larger conjoined mm-scale cavities (e.g. Fig. 7a). The bubble-like morphology of these voids (Fig. 7b) suggest that their genesis involved gases either evolved or introduced during the welding process. One potential source of these gases is the cerium-rich oxide inclusions found embedded throughout the parent material, which may have been thermally decomposed by welding heat. Oxygen evolved from the thermal decomposition of one or more of these inclusions could diffuse through the molten weld zone to contribute to the

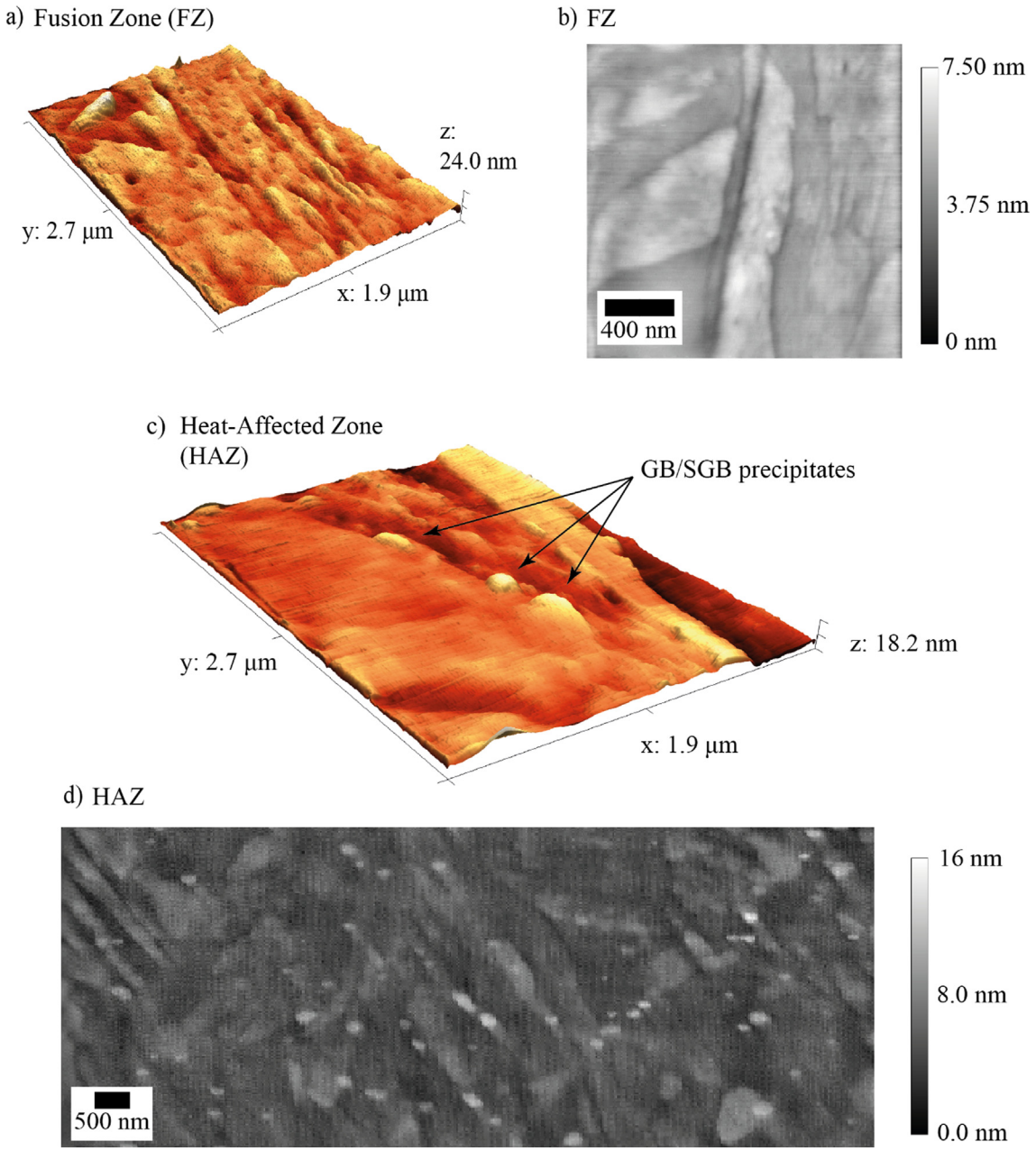

Fig. 10. Selected large area HS-AFM images of the FZ (a, b) and the HAZ (c, d) with some large precipitates highlighted.

growth of these large voids. This theory is supported by the presence of spatter-like ceria residues on the interior surface of several voids (Fig. 7b, highlighted by arrows).

These cerium-rich inclusions may have been introduced during steelmaking as cerium oxide is employed as a refractory lining by some high-temperature foundry crucibles [32]. Ceria nanoparticles are under consideration for use in oxide-dispersed reduced-activation steels, thus the observed inclusions are unlikely to negatively affect the reduced-activation performance of Eurofer 97 [33]. However, their presence in other, non-welded samples of Eurofer 97 suggests that they are widespread, and their potential role in void genesis during LKW of Eurofer 97 is cause for concern. Further insights into the origin of these inclusions and their role in void genesis may be gained by performing chemical analysis of inclusions and void-borne residues using secondary ion mass spectrometry (SIMS) or Raman spectroscopy.

5. Conclusions

The high-temperature environment of the DEMO fusion reactor poses a unique challenge for the novel welded joints of the plasma-facing FW. The capability to predict the long-term performance of these welds under reactor-relevant conditions would aid the continuing development of advanced welding techniques and could contribute to the design safety case of the DEMO reactor. This paper demonstrates that coupling FETA with precipitate kinetics modelling is a promising approach to modelling these novel welded joints.

The extents of each region of the LKW Eurofer 97 weld and the general trends in precipitate nucleation and growth throughout the welded regions have been successfully predicted. However, further work is required to refine the precipitate kinetics models and improve their predictions of precipitate diameters. The devel-

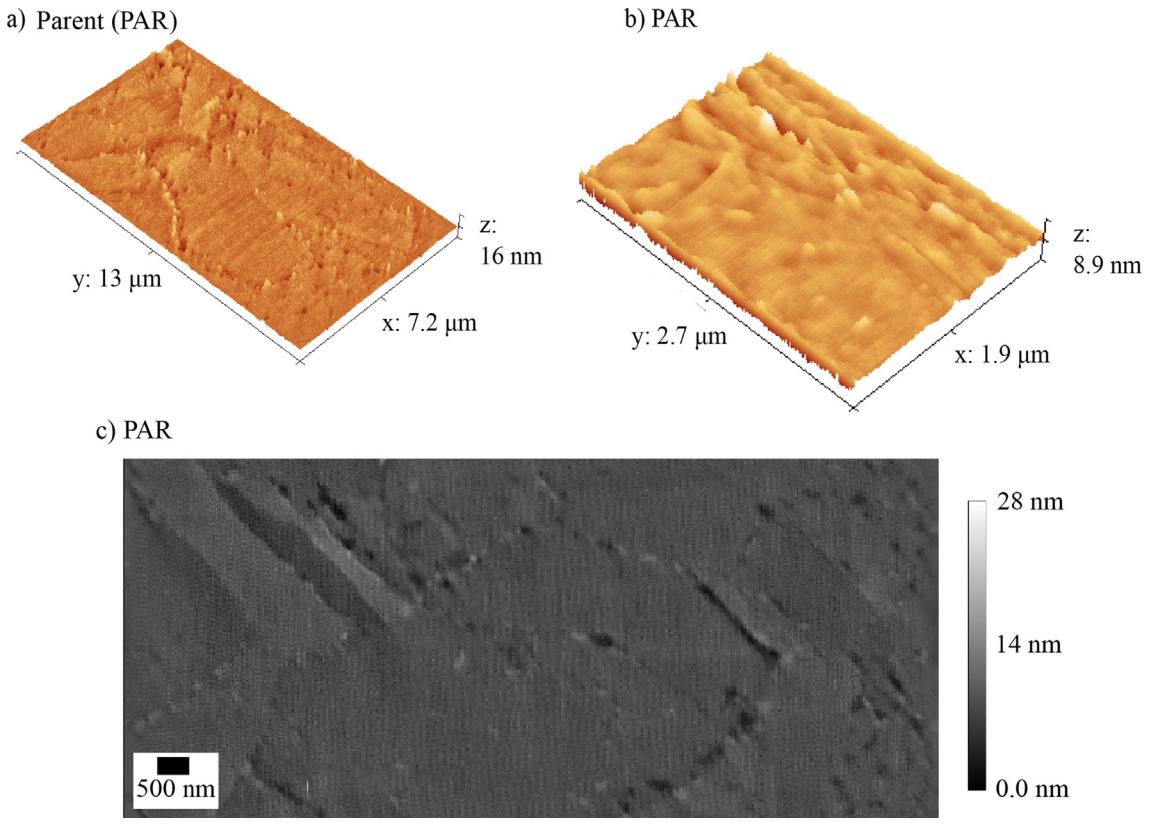

Fig. 11. Selected large area HS-AFM images of the parent material.

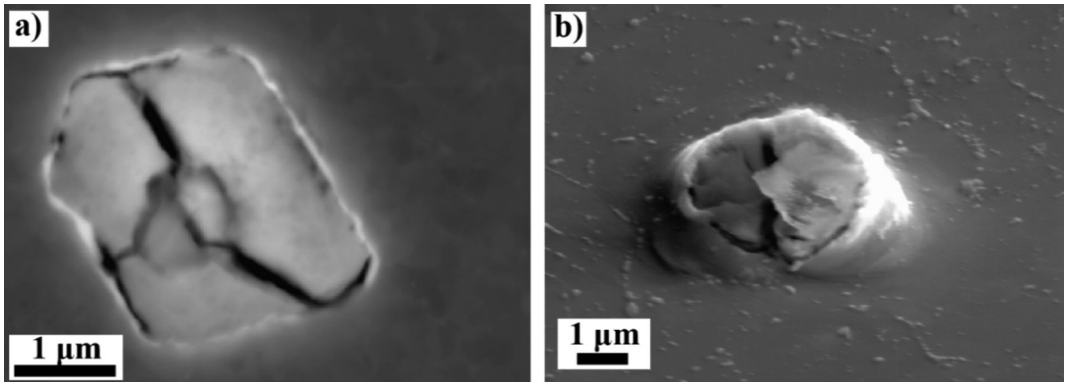

Fig. 12. AsB micrographs of spheroidal inclusions in (a) the parent material of the LKW Eurofer 97 and (b) a non-welded sample of Eurofer 97 used for a transient thermal ageing study.

opment of accurate models for Eurofer 97′s grain and sub-grain growth kinetics is expected to greatly improve the modelling results. These improvements would, it is hoped, enable further exploratory modelling studies to be conducted on the effects of post-weld heat treatments (PWHTs), and the effects of long-term isothermal and transient thermal ageing.

The large voids and ceria inclusions observed in LKW Eurofer 97 are likely to be problematic for both the fabrication and long-term operation of DEMO's FW. Their origins and the theorised causal link between them described herein require further investigation. Future work on the chemical assay of ceria inclusions before and after keyhole welding is recommended.

Data availability

Data will be made available on request.

Declaration of Competing Interest

The authors declare that they have no known competing financial interests or personal relationships that could have appeared to influence the work reported in this paper.

Acknowledgements

The authors would like to thank UKAEA for providing a representative specimen of laser-welded Eurofer 97. This work was supported by the UK EPSRC via Nuclear Energy Futures CDT (EPSRC

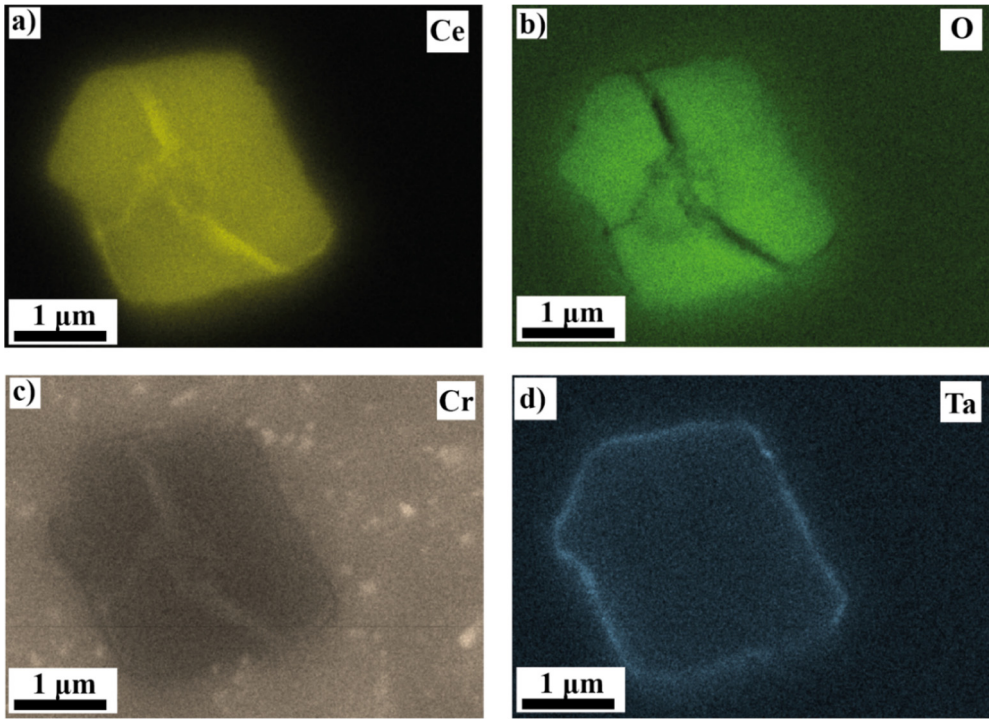

Fig. 13. Element-specific EDX maps of the cerium-rich inclusion shown in Fig. 12a.

grant EP/S023844/1) and the University of Bristol. Dr Chris Jones is thanked for their assistance.

References

[1] H. Tanigawa et al., Development of benchmark reduced activation ferritic/martensitic steels for fusion energy applications, Nucl. Fusion 57 (9) (Jun. 2017), https://doi.org/10.1088/1741-4326/57/9/092004 092004.
[2] P. Jung, J. Henry, J. Chen, Tensile properties of candidate structural materials for high power spallation sources at high helium contents, J. Nucl. Mater. 343 (1) (Aug. 2005) 275–284, https://doi.org/10.1016/j.jnucmat.2004.11.018.
[3] C. Cabet, F. Dalle, E. Gaganidze, J. Henry, H. Tanigawa, Ferritic-martensitic steels for fission and fusion applications, J. Nucl. Mater. 523 (Sep. 2019) 510–537, https://doi.org/10.1016/j.jnucmat.2019.05.058.
[4] M. Rieth, "Material Property Handbook on Eurofer 97," Eurofusion Power Plant Physics and Technology Dept., MAT-1.2.1-T006-D002, 2016.
[5] X. Chen et al., Mechanical properties and microstructure characterization of Eurofer97 steel variants in EUROfusion program, Fusion Eng. Des. 146 (Sep. 2019) 2227–2232, https://doi.org/10.1016/j.fusengdes.2019.03.158.
[6] S. Kumar, C. Pandey, A. Goyal, A microstructural and mechanical behavior study of heterogeneous P91 welded joint, Int. J. Press. Vessel. Pip. 185 (Aug. 2020), https://doi.org/10.1016/j.ijpvp.2020.104128 104128.
[7] D. De Meis, "Structural materials for DEMO," ENEA - Italian National Agency for New Technologies, Energy and Sustainable Economic Development, 2015.
[8] L. Forest et al., Status of the EU DEMO breeding blanket manufacturing R&D activities, Fusion Eng. Des. 152 (Mar. 2020), https://doi.org/10.1016/j.fusengdes.2019.111420 111420.
[9] F. Edemetti, E. Martelli, A. Tassone, G. Caruso, A.D. Nevo, DEMO WCLL breeding zone cooling system design: Analysis and discussion, Fusion Eng. Des. 146 (Sep. 2019) 2632–2638, https://doi.org/10.1016/j.fusengdes.2019.04.063.
[10] A. Tassone et al., Recent Progress in the WCLL Breeding Blanket Design for the DEMO Fusion Reactor, IEEE Trans. Plasma Sci. 46 (5) (May 2018) 1446–1457, https://doi.org/10.1109/TPS.2017.2786046.
[11] E. Martelli et al., Advancements in DEMO WCLL breeding blanket design and integration, Int. J. Energy Res. 42 (1) (2018) 27–52, https://doi.org/10.1002/er.3750.
[12] C. Bachmann et al., Key design integration issues addressed in the EU DEMO pre-concept design phase, Fusion Eng. Des. 156 (Jul. 2020), https://doi.org/10.1016/j.fusengdes.2020.111595 111595.
[13] J. Moon, J.-J. Lee, C.-H. Lee, Reheating cracking susceptibility in the weld heat-affected zone of reduced activation ferritic-martensitic steels and the effect of Cr content, J. Nucl. Mater. 542 (Dec. 2020), https://doi.org/10.1016/j.jnucmat.2020.152499 152499.
[14] V. Thomas Paul, S. Saroja, S.K. Albert, T. Jayakumar, E. Rajendra Kumar, Microstructural characterization of weld joints of 9Cr reduced activation ferritic martensitic steel fabricated by different joining methods, Mater. Characterizat. 96 (2014) 213–224, https://doi.org/10.1016/j.matchar.2014.08.013.
[15] L.M. Giancarli et al., Overview of recent ITER TBM Program activities, Fusion Eng. Des. 158 (Sep. 2020), https://doi.org/10.1016/j.fusengdes.2020.111674 111674.
[16] S. Kirk, W. Suder, K. Keogh, T. Tremethick, A. Loving, Laser welding of fusion relevant steels for the European DEMO, Fusion Eng. Des. 136 (Nov. 2018) 612–616, https://doi.org/10.1016/j.fusengdes.2018.03.039.
[17] S. Kirk, W. Suder, K. Keogh, "Laser Welding of P91 & EUROFER97 steels for fusion reactor coolant pipes," presented at the Nuclear Materials Conference, Nov. 2016. https://doi.org/10.13140/RG.2.2.26630.16967.
[18] F. Maviglia et al., Integrated design strategy for EU-DEMO first wall protection from plasma transients, Fusion Eng. Des. 177 (Apr. 2022), https://doi.org/10.1016/j.fusengdes.2022.113067 113067.
[19] C. Pandey, M.M. Mahapatra, Effect of Heat Treatment on Microstructure and Hot Impact Toughness of Various Zones of P91 Welded Pipes, J. Mater. Eng. Perform 25 (6) (Jun. 2016) 2195–2210, https://doi.org/10.1007/s11665-016-2064-x.
[20] M. Zmitko et al., The European ITER Test Blanket Modules: EUROFER97 material and TBM's fabrication technologies development and qualification, Fusion Eng. Des. 124 (Nov. 2017) 767–773, https://doi.org/10.1016/j.fusengdes.2017.04.051.
[21] N. Taylor et al., Resolving safety issues for a demonstration fusion power plant, Fusion Eng. Des. 124 (Nov. 2017) 1177–1180, https://doi.org/10.1016/j.fusengdes.2017.02.018.
[22] A. Harte, H. Dawson, D. Bowden, R. Spencer, S. Kirk, M. Gorley, Deformation heterogeneity in laser-welded Eurofer, Fusion Eng. Des. 161 (Dec. 2020), https://doi.org/10.1016/j.fusengdes.2020.111860 111860.
[23] A.P. Tadamalle, Y.P. Reddy, E. Ramjee, V. Reddy, Evaluation of Nd: YAG Laser Welding Efficiencies for 304L Stainless Steel, Procedia Mater. Sci. 6 (2014) 1731–1739, https://doi.org/10.1016/j.mspro.2014.07.160.
[24] M. Slezak, M. Warzecha, Investigations of Liquid Steel Viscosity and Its Impact as the Initial Parameter on Modeling of the Steel Flow through the Tundish, Materials 13(21) (2020) https://doi.org/10.3390/ma13215025, Art. no. 21.
[25] A. Kalup, M. Žaludová, S. Zlá, L. Drozdová, L. Válek, B. Smetana, Latent heats of melting and solidifying of real steel grades, in: Proceedings of the 23rd International Conference on Metallurgy and Materials (METAL-2014), Brno, Czech Republic, 2014, pp. 21–32.
[26] A.D. Schino, C. Testani, L. Pilloni, Effect of thermo-mechanical parameters on the mechanical properties of Eurofer97 steel for nuclear applications, Open Eng. 8 (1) (Oct. 2018) 349–353, https://doi.org/10.1515/eng-2018-0040.
[27] D. Kumar et al., The Effects of Fusion Reactor Thermal Transients on the Microstructure of Eurofer-97 Steel, J. Nucl. Mater. (2021) 153084 https://doi.org/10.1016/j.jnucmat.2021.153084.
[28] D. Brimbal et al., Microstructural characterization of Eurofer-97 and Eurofer-ODS steels before and after multi-beam ion irradiations at JANNUS Saclay facility, J. Nucl. Mater. 465 (Oct. 2015) 236–244, https://doi.org/10.1016/j.jnucmat.2015.05.045.

[29] M. Klimenkov, R. Lindau, E. Materna-Morris, A. Möslang, TEM characterization of precipitates in EUROFER 97, Prog. Nucl. Energy 57 (May 2012) 8–13, https://doi.org/10.1016/j.pnucene.2011.10.006.
[30] A.D. Warren, A.I. Martinez-Ubeda, O.D. Payton, L. Picco, T.B. Scott, Preparation of Stainless Steel Surfaces for Scanning Probe Microscopy, Microscopy Today 24 (3) (May 2016) 52–55, https://doi.org/10.1017/S1551929516000341.
[31] K.H. Dhandha, V.J. Badheka, Effect of activating fluxes on weld bead morphology of P91 steel bead-on-plate welds by flux assisted tungsten inert gas welding process, J. Manuf. Process. 17 (Jan. 2015) 48–57, https://doi.org/10.1016/j.jmapro.2014.10.004.
[32] M. O'Brien, M. Akinc, Role of Ceria in Enhancing the Resistance of Aluminosilicate Refractories to Attack by Molten Aluminum Alloy, J. Am. Ceram. Soc. 72 (Mar. 2005) 896–904, https://doi.org/10.1111/j.1151-2916.1989.tb06241.x.
[33] J. Gong, H. Liao, K. Zhang, X. Wang, Heat treatment optimization of China low-activation ferritic/martensitic steel with cerium addition, Fusion Eng. Des. 158 (Sep. 2020), https://doi.org/10.1016/j.fusengdes.2020.111696 111696.